

Coexistence of antiferromagnetism and superconductivity in Mn/Nb(110)Roberto Lo Conte^{1,*}, Maciej Bazarnik^{1,2,†}, Krisztián Palotás^{3,4,5}, Levente Rózsa⁶, László Szunyogh^{4,7},
André Kubetzka¹, Kirsten von Bergmann¹, and Roland Wiesendanger¹¹*Department of Physics, University of Hamburg, D-20355 Hamburg, Germany*²*Institute of Physics, Poznan University of Technology, Piotrowo 3, 60-965 Poznan, Poland*³*Institute for Solid State Physics and Optics, Wigner Research Center for Physics, H-1525 Budapest, Hungary*⁴*Department of Theoretical Physics, Institute of Physics, Budapest University of Technology and Economics, Műegyetem rkp. 3., H-1111 Budapest, Hungary*⁵*MTA-SZTE Reaction Kinetics and Surface Chemistry Research Group, University of Szeged, H-6720 Szeged, Hungary*⁶*Department of Physics, University of Konstanz, D-78457 Konstanz, Germany*⁷*MTA-BME Condensed Matter Research Group, Budapest University of Technology and Economics, H-1111 Budapest, Hungary*

(Received 18 August 2021; revised 20 February 2022; accepted 23 February 2022; published 10 March 2022)

We report on the structural, magnetic, and superconducting properties of single and double atomic layers of Mn on a clean and unreconstructed Nb(110) substrate. Low-temperature scanning tunneling spectroscopy measurements reveal a proximity-induced superconducting state and in-gap Yu-Shiba-Rusinov bands in the Mn thin films, which are found to grow pseudomorphically on the Nb surface. Spin-polarized scanning tunneling microscopy measurements reveal a $c(2 \times 2)$ antiferromagnetic (AFM) order in the Mn layers, with an out-of-plane spin orientation. First-principles density functional theory calculations confirm the experimentally observed magnetic state, which is understood as the consequence of a strong intralayer and interlayer nearest-neighbor AFM exchange coupling. These results are expected to be of importance for the design of superconducting AFM spintronic systems and quantum information technologies.

DOI: [10.1103/PhysRevB.105.L100406](https://doi.org/10.1103/PhysRevB.105.L100406)

The concepts of topological superconductivity and superconducting spintronics sparked recent research efforts in combining magnetic and superconducting materials. It is well understood that, when the spin of a magnetic impurity interacts with a superconducting condensate, Yu-Shiba-Rusinov (YSR) in-gap bound states emerge [1–4]. This picture becomes more complex when magnetic adatoms are put together to form one-dimensional (1D) atomic chains, where YSR states start hybridizing, giving rise to dispersive energy bands and, potentially, Majorana end modes [5–11]. Analogously, it is expected that, when two-dimensional magnetic islands on a superconductor are considered, multiple YSR bands are formed, and propagating topological edge modes can emerge [12–14]. Furthermore, spin-triplet pairing amplitudes can exist in magnet/superconductor hybrids [15,16], resulting in spin-polarized supercurrents [17–19] which are potentially applicable in the design of superconducting digital and quantum circuits [20,21] and ultralow dissipation magnetic domain wall memories [22] and logics [23].

Recently, a successful recipe for the preparation of clean and unreconstructed Nb(110) surfaces was demonstrated [24], making it possible to study the properties of magnetic $3d$ transition metal impurities [25,26] and atomic chains [10] on the s -wave elemental superconductor with the highest critical

temperature ($T_C = 9.25$ K). Interestingly, the study of artificially built Mn atomic chains on top of a clean Nb(110) substrate has shown the emergence of p -wave superconductivity [10] and the evidence of interacting Majorana modes [27]. Those results on atomic-scale systems motivate the investigation of extended Mn films on top of Nb substrates, where equally interesting effects could emerge. However, this would be possible only if the proximity-induced superconductivity is not suppressed by the exchange field of the two-dimensional (2D) magnetic system. It has been previously shown that magnetic impurities on a superconducting Pb surface strongly suppress the superconducting phase above a certain concentration level [28]. Accordingly, it is important to understand the feasibility of growing magnetic $3d$ transition metal films on Nb substrates, where proximity-induced superconductivity and magnetic order coexist. In 1D chains of Mn on Nb(110), the superconductivity survives [10], making Mn an auspicious starting point for thin-film studies. Furthermore, the knowledge of the exact spin texture present in the magnetic layer is key for the understanding of potential emergent electronic properties [29,30], motivating experimental investigations via scanning probe techniques with magnetic sensitivity and atomic resolution.

Here, we report on the study of the structural, magnetic, and superconducting properties of Mn ultrathin films deposited on a clean Nb(110) surface. Low-energy scanning tunneling spectroscopy (STS) measurements are carried out to characterize the superconducting state of Mn ultrathin films. Spin-polarized scanning tunneling microscopy

*rloconte.magnetism@gmail.com

†mbazarni@physnet.uni-hamburg.de

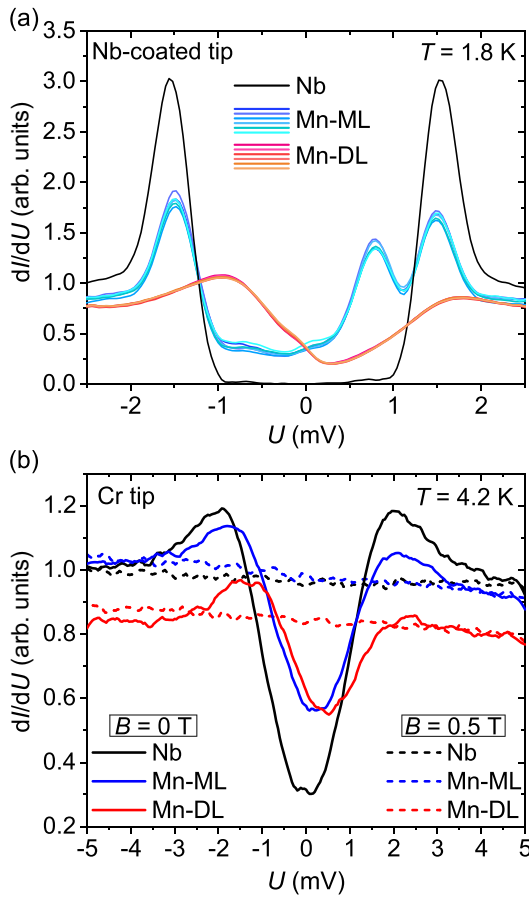


FIG. 1. Local density of states (LDOS) characterization via scanning tunneling spectroscopy (STS). (a) Normalized low bias dI/dU spectra from the bare Nb surface (black), Mn-ML (blue shades), and Mn-DL (red shades) acquired at $T = 1.8$ K with a Nb-coated scanning tunneling microscopy (STM) tip. Each curve is a point spectrum over the sample surface, after numerical deconvolution of the superconducting tip density of states (DOS) [35,38–40]. The different point spectra on the Mn-ML and Mn-DL are acquired on a line approximately along the $[\bar{1}10]$ ($[\bar{1}11]$) crystallographic direction, with a distance of 290 (250) pm between consecutive points on the Mn-ML (Mn-DL). (b) Normalized low-bias dI/dU spectra from the bare Nb surface (black), Mn-ML (blue), and Mn-DL (red) acquired at $T = 4.2$ K with a Cr tip. Stabilization parameters: $I = 1$ nA, $U = 20$ mV, modulation $\Delta U = 50$ μ V.

(SP-STM) [31] is used for the direct imaging of the morphology and the magnetic ground states of Mn monolayers (MLs) and double layers (DLs). The experimentally observed magnetic state is successfully reproduced by first-principles density functional theory (DFT) calculations.

The Mn films are grown by physical vapor deposition on a clean and unreconstructed Nb(110) surface, resulting in samples where the ML and DL are available for experimental investigation (more details in the Supplemental Material [32]). Low-bias STS measurements performed over the bare Nb(110) surface as well as the Mn-ML and Mn-DL with a superconducting Nb-coated STM tip are shown in Fig. 1(a). On the one hand, the STS spectrum acquired over the bare Nb surface (black curve) confirms its superconducting state, as shown by the presence of symmetric

coherence peaks ($U_{cp} = \pm 1.55$ mV) and the zero differential conductance dI/dU between them [24]. On the other hand, the point spectra acquired at different positions over the Mn-ML (blue curves) and Mn-DL (red curves) show a nonzero differential conductance in the superconducting gap of the Nb. For the Mn-ML, we observe the coherence peaks at $U = \pm 1.5$ mV with a reduced amplitude and an additional in-gap peak at $U = +0.8$ mV, while the coherence peaks are strongly suppressed for the Mn-DL and a broad in-gap peak is observed at $U = -0.95$ mV. These observations could be potentially explained by the following scenarios: (i) simultaneous measurement of the superconducting local density of states (LDOS) of the Nb substrate and the metallic LDOS of the Mn layers, (ii) Kondo resonances, (iii) low-energy spin excitations, or (iv) in-gap YSR bands. To identify the origin of the observed LDOS in Fig. 1(a), additional STS spectra are acquired with an STM tip with a magnetic-field-independent density of states (DOS) while the sample is in the superconducting ($B = 0$ T) and normal conducting ($B = 0.5$ T) states, as shown in Fig. 1(b). The STS measurements on the superconducting sample confirm a symmetric dI/dU curve for the bare Nb and the additional in-gap states in the Mn films, like what was observed for single Mn adatoms on a Nb(110) substrate at $T \sim 4$ K [33]. Comparison with Fig. 1(a) suggests that the apparent intensity of the in-gap states partially depends on the probing tip. Featureless spectra are obtained for the normal conducting sample. The last observation allows us to rule out the first interpretation since the measured Mn LDOS in the normal state has no features in the energy range of the superconducting gap. Based on the dI/dU curves shown in Fig. 1, it also seems unlikely that the observed in-gap features are related to potential Kondo resonances or low-energy spin excitations. Kondo resonances for magnetic impurities on metallic surfaces usually appear as wide (~ 10 meV) features around the Fermi level [34,35]. Furthermore, even when Kondo resonances [36] and low-energy spin excitations [37] have narrow line widths, the associated spectral features survive at magnetic fields of several Tesla, while the data shown in Fig. 1(b) clearly demonstrate that this is not the case for the in-gap states reported in this paper. Accordingly, we conclude that our STS measurements show proximity-induced superconductivity in the Mn thin films and the presence of in-gap YSR bands. This points to the coexistence of magnetic and superconducting phases in the Mn films and motivates the structural and magnetic characterization discussed below.

In Fig. 2(a), a large-scale topographic image of one of the prepared samples shows an almost fully developed Mn-ML partially covered by small patches of DL, as the result of a step-flow growth. In Fig. 2(b), a line profile shows the apparent height of the deposited thin film over the Nb(110) substrate. Figure 2(c) reports the atomic structure of the Mn-ML, showing a body-centered cubic [bcc(110)] symmetry and interatomic distances along the $[001]$, a_{Mn} , and $[\bar{1}10]$, $b_{Mn} = \sqrt{2}a_{Mn}$, directions, which are in agreement with those of the Nb(110) surface ($a_{Nb} = 330$ pm, $b_{Nb} = 467$ pm), demonstrating a pseudomorphic growth. Finally, in Fig. 2(d), the atomic structures of Mn-ML (top left) and Mn-DL (bottom right) are directly compared. The pseudomorphic growth is maintained also in the DL patches.

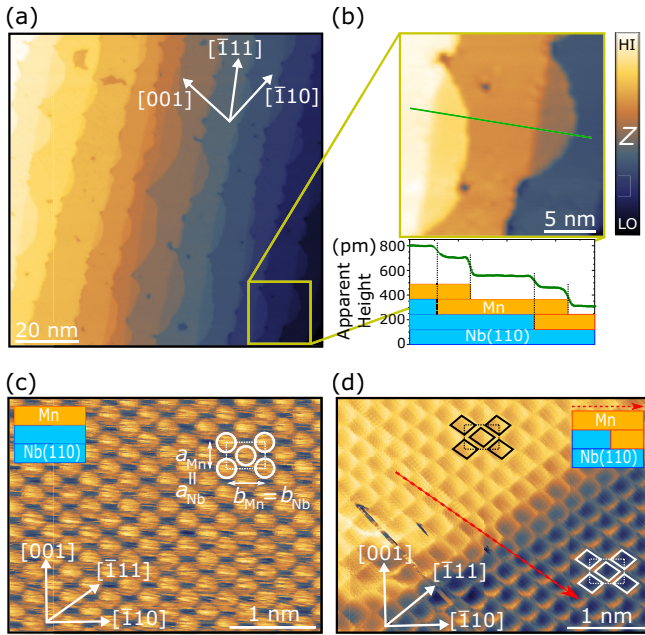


FIG. 2. Structural properties of Mn-ML and Mn-DL on Nb(110) at $T = 4.2$ K. (a) Topographic scanning tunneling microscopy (STM) image of 1.2 ML of Mn on the Nb(110) surface ($U = 20$ mV, $I = 2$ nA). (b) Zoom-in from the image in (a) with a line profile showing the apparent height of the different layers on the surface of the sample. (c) Atomically resolved topographic STM image of Mn-ML ($U = 30$ mV, $I = 2$ nA), showing a bcc(110) surface symmetry. (d) Atomically resolved topographic image (via atomic manipulation imaging mode [41]) of both Mn-ML and Mn-DL ($U = 3$ mV, $I = 10$ nA), showing the same surface symmetry and interatomic distances.

Next, we investigate the magnetic state of the Mn thin films via SP-STM. Figure 3(a) shows a low-bias topography image of the Mn-ML, where the atomic structure and the magnetic contrast are simultaneously resolved. The magnetic contrast in Fig. 3(a) reveals the presence of a spin texture which is consistent with a $c(2 \times 2)$ antiferromagnetic (AFM) ground state, as sketched in the inset. Due to the symmetry of the bcc(110) Mn surface, the $c(2 \times 2)$ AFM state appears as a rowlike pattern in the SP-STM images [42], where spin-up and spin-down ferromagnetic (FM) rows along the [001] direction alternate with each other along the $[\bar{1}10]$ direction. To corroborate this finding, the Heisenberg exchange interactions between the spins in the Mn-ML were calculated using the spin-cluster expansion (SCE) [43] as implemented in the screened Korrington-Kohn-Rostoker (SKKR) DFT method [44] (see Ref. [32] for calculation details and Refs. [45–52] for more references). As shown in Fig. 3(b), the AFM nearest-neighbor (NN) exchange coupling along the $[\bar{1}11]$ direction ($d_1 = \sqrt{3}/2a_{\text{Mn}}$) and the FM next-NN (NNN) exchange coupling along the [001] direction ($d_2 = a_{\text{Mn}}$) stabilize a $c(2 \times 2)$ AFM ground state, in agreement with the experimental results. Furthermore, an out-of-plane magnetic easy axis is predicted for the Mn-ML, which would establish an AFM ground state as the one shown in the sketch in Fig. 3(c). The spin orientation in the Mn-ML is experimentally verified by

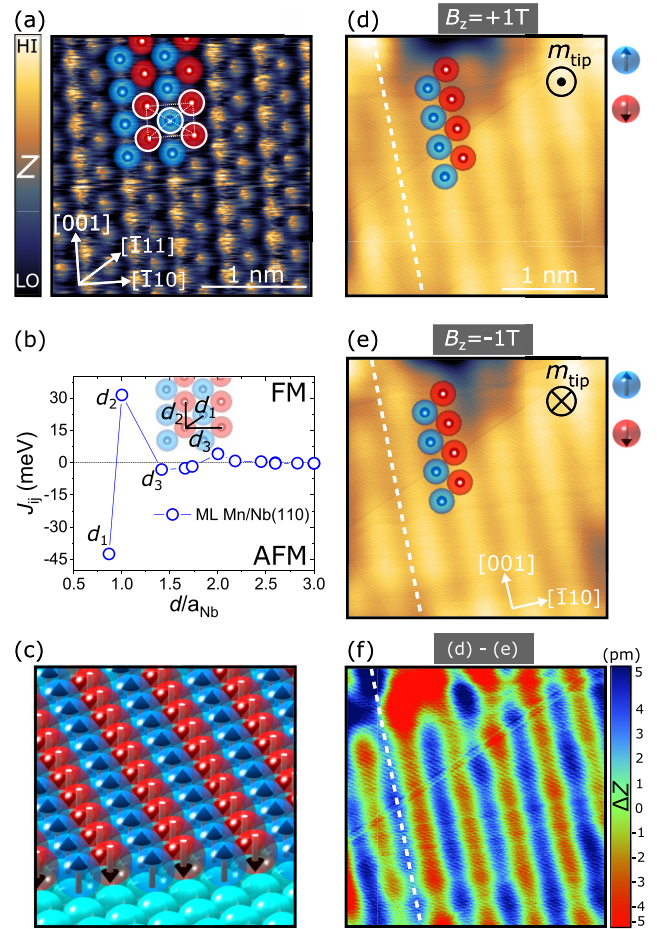


FIG. 3. Magnetism of Mn-ML on Nb(110) at $T = 4.2$ K. (a) Spin-polarized scanning tunneling microscopy (SP-STM) image of Mn-ML ($U = 30$ mV, $I = 2$ nA) revealing the presence of the $c(2 \times 2)$ antiferromagnetic (AFM) ground state (unit cell in white). (b) Calculated Heisenberg exchange interactions J_{ij} as a function of the interatomic distance d , predicting an AFM coupling between nearest-neighbor (NN) atoms along $[\bar{1}11]$ and a ferromagnetic (FM) coupling between next-nearest-neighbor (NNN) atoms along [001]. a_{Nb} is the bulk Nb lattice constant and d_1 , d_2 , and d_3 indicate the NN, NNN, and third-NN distance, respectively. (c) Sketch of the $c(2 \times 2)$ AFM ground state of the Mn-ML on Nb(110). Blue and red spheres indicate spin-up and spin-down atoms, respectively. (d) and (e) SP-STM image of Mn-ML obtained with a soft magnetic tip in a $+1$ T/ -1 T out-of-plane magnetic field ($U = 20$ mV, $I = 5$ nA). (f) Computed difference image (d)–(e), revealing the out-of-plane magnetic contrast in the Mn-ML.

imaging its magnetic state with a soft magnetic tip, whose magnetic moment at its apex m_{tip} could be easily reoriented via an external magnetic field. Figures 3(d) and 3(e) report the magnetic contrast observed in the Mn-ML via the soft magnetic tip while an out-of-plane magnetic field $B_z = +1$ and -1 T is applied, respectively. The two images show the same rowlike pattern but with an inverted contrast, which is highlighted by the computed difference (d)–(e) image presented in Fig. 3(f). All the experimental evidence confirms

an AFM ground state with an out-of-plane easy axis, in full agreement with the DFT calculations.

To access the magnetic state of both the ML and DL in the same scan, we acquire spin-resolved dI/dU maps at $U = +1.9$ V with a bulk Cr tip (more details in the Supplemental Material [32]). Figure 4(a) shows a topographic STM image of the surface of the sample where both Mn-ML and Mn-DL are present. The spin-resolved dI/dU map in Fig. 4(b) shows the AFM pattern in both Mn-ML (pink) and Mn-DL (green). The dashed black arrow shows how the FM row on the ML continues over the DL island situated on the lower atomic terrace, indicating a continuity in the spin orientation. The spin-resolved dI/dU map in Fig. 4(b) is acquired with a small out-of-plane field of $+0.5$ T. To test the robustness of the AFM state to high external fields, dI/dU maps with $B_z = +9$ T are acquired as well [see Fig. 4(c) and 4(d)], showing an unperturbed AFM state. Furthermore, an inverted magnetic contrast is observed for the top and bottom atomic layers of Mn-DL [see dashed black arrow in Fig. 4(d)]. This suggests the presence of an interlayer NN AFM spin alignment. The exchange interactions in the Mn-DL were also calculated using SCE in the SKKR method and reported in Fig. 4(e). A particularly strong NN AFM exchange coupling is predicted to dominate the interlayer magnetic coupling (green symbols + dashed line). In addition, both bottom (black symbols + solid line) and top (gold symbols + dotted line) atomic layers are predicted to be characterized by an intralayer AFM coupling between NN atoms and a weaker FM coupling between NNN atoms, as for the ML case. As a result, the predicted magnetic state is a type-I AFM ground state, with the NNs pointing antiparallel inside the layers as well as between the layers, as schematically shown in Fig. 4(f), in full agreement with our experimental observations. It is worth noting that, in contrast to what was previously observed in Mn films on W(110) [53], noncollinear spin textures are not observed here. The main reason is the much smaller Dzyaloshinsky-Moriya interactions—due to the moderate spin-orbit coupling in the Nb substrate—which are not strong enough to compete with the magnetic anisotropy in the system [32].

Considering the established AFM state of the Mn thin films on the Nb substrate, it is possible to discuss more in depth the observed dI/dU spectra reported in Fig. 1(a). The line spectra acquired over Mn-ML (blue curves) and Mn-DL (red curves) cut across several magnetic unit cells, without showing any dependence of the in-gap DOS features over the local magnetization. A dependence of the intensity of the in-gap features over the local magnetic texture is not excluded. However, this is inaccessible with the non-spin-sensitive Nb-coated tip used in this paper for maximizing the energy resolution of the acquired spectra. It is also worth commenting that the AFM order of the Mn thin films could play a crucial role for the establishment of the observed proximity-induced superconductivity in our two-dimensional magnet. An AFM order is in principle compatible with the presence of singlet Cooper pairs [54]. Such a scenario was also discussed for the superconducting FeTe ML on Bi_2Te_3 [55], where the superconducting state was found to coexist with a bicollinear AFM order. Manna *et al.* [55] attributed such a coexistence to the fact that the size of the Cooper pairs was larger than the periodicity of the AFM order in their FeTe ML, allowing

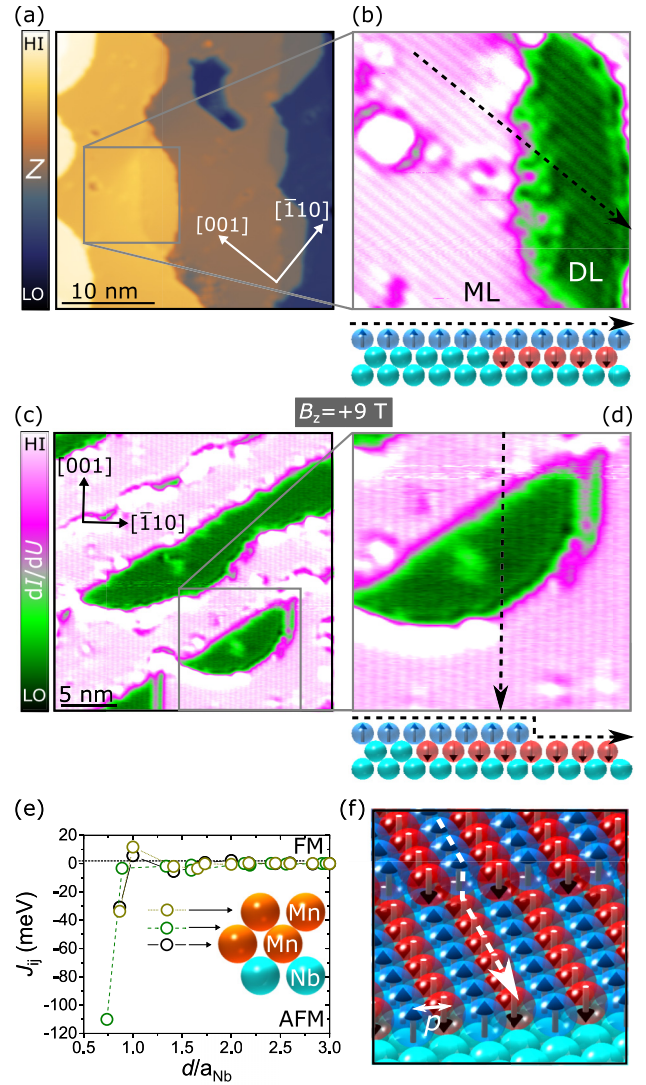


FIG. 4. Magnetism of Mn-ML and Mn-DL on Nb(110) at $T = 4.2$ K. (a) Topographic scanning tunneling microscopy (STM) image and (b) spin-resolved differential conductance dI/dU map of Mn-ML and Mn-DL. The spin-resolved dI/dU map reveals the presence of a $c(2 \times 2)$ antiferromagnetic (AFM) state in both layers, with the magnetic contrast conserved across the ML/DL boundary. (c) Spin-resolved dI/dU map of the Mn film in a $+9$ T out-of-plane magnetic field, showing an unperturbed AFM state. (d) Zoomed-in dI/dU map confirming the conservation of the magnetic contrast across the ML/DL boundary and showing the inversion of the magnetic contrast between the top and the bottom atomic layer in the Mn-DL ($U = 1.9$ V, $\Delta U = 20$ mV, $I = 5$ nA, bulk Cr tip). (e) Calculated Heisenberg exchange interactions for the Mn-DL as a function of the interatomic distance d for the bottom (black symbols) and top (gold symbols) Mn layers as well as the interlayer (green symbols) coupling. The latter shows a strong AFM coupling between nearest-neighbor (NN) atoms, which drives the inversion of the spin texture between the bottom and the top atomic layer. (f) Sketch of the AFM state of the bottom and top atomic layer in the Mn-DL on Nb(110). Blue and red spheres indicate spin-up and spin-down atoms, respectively. The white dashed arrow follows the inverted spin state in the top and bottom atomic layer of the Mn-DL, due to a lateral shift of $p = b_{\text{Mn}}/2$ in the $[\bar{1}10]$ crystallographic direction.

the antiparallel alignment between the spins in the Cooper pairs to survive without phase separation. Even though the superconductivity in the FeTe ML is not induced by proximity, the coexistence of superconductivity and antiferromagnetism is analogous to the case observed in our hybrid system, and the same argument could be used in this case, where the size of the Cooper pairs is expected to be comparable with the coherence length in the Nb substrate $\xi \sim 40$ nm [56], and the periodicity of the AFM order in the Mn film is <1 nm. This clearly establishes Mn thin films on Nb as a promising hybrid system for the study of electronic and spin-transport effects in a superconducting antiferromagnet [15,16], and the present atomic-scale characterization provides a solid basis for the understanding of potential emergent effects applicable in superconducting AFM spintronics and quantum information technology.

R.L.C. and R.W. acknowledge financial support by the European Union via a Marie Skłodowska-Curie Fellowship (Grant No. 748006-SKDWONTRACK). R.L.C., A.K.,

M.B., and K.v.B. acknowledge financial support by the Deutsche Forschungsgemeinschaft (German Research Foundation) Projects No. 459025680, No. 408119516, and No. 418425860. R.W. acknowledges funding by the European Union via ERC Advanced Grant ADMIRE (project no. 786020). K.P., L.R., and L.Sz. acknowledge financial support by the National Research, Development, and Innovation Office (NRDI) of Hungary under Projects No. FK124100 and No. K131938. K.P. and L.Sz. acknowledge support by the Ministry of Innovation and Technology and the NRDI Office within the Quantum Information National Laboratory of Hungary. K.P. acknowledges the János Bolyai Research Grant of the Hungarian Academy of Sciences (BO/292/21/11) and the New National Excellence Program of the Ministry for Innovation and Technology from the National Research, Development, and Innovation Office (NRDI) Fund (Grant No. ÚNKP-21-5-BME-345). The authors would like to thank J. Wiebe, L. Schneider, P. Beck, T. Hänke, and E. Mascot for the fruitful discussions.

R.L.C. and M.B. contributed equally to this paper.

-
- [1] Y. Luh, *Acta Phys. Sin.* **21**, 75 (1965).
 [2] H. Shiba, *Prog. Theor. Phys.* **40**, 435 (1968).
 [3] A. I. Rusinov, *JETP Lett.* **9**, 85 (1969).
 [4] B. W. Heinrich, J. I. Pascual, and K. J. Franke, *Prog. Surf. Sci.* **93**, 1 (2018).
 [5] S. Nadj-Perge, I. K. Drozdov, J. Li, H. Chen, S. Jeon, J. Seo, A. H. MacDonald, B. A. Bernevig, and A. Yazdani, *Science* **346**, 602 (2014).
 [6] B. E. Feldman, M. T. Randeria, J. Li, S. Jeon, Y. Xie, Z. Wang, I. K. Drozdov, B. Andrei Bernevig, and A. Yazdani, *Nat. Phys.* **13**, 286 (2017).
 [7] F. Pientka, Y. Peng, L. Glazman, and F. Von Oppen, *Phys. Scr.* **T164**, 014008 (2015).
 [8] H. Kim, A. Palacio-Morales, T. Posske, L. Rózsa, K. Palotás, L. Szunyogh, M. Thorwart, and R. Wiesendanger, *Sci. Adv.* **4**, eaar5251 (2018).
 [9] L. Schneider, S. Brinker, M. Steinbrecher, J. Hermenau, T. Posske, M. dos Santos Dias, S. Lounis, R. Wiesendanger, and J. Wiebe, *Nat. Commun.* **11**, 4707 (2020).
 [10] L. Schneider, P. Beck, T. Posske, D. Crawford, E. Mascot, S. Rachel, R. Wiesendanger, and J. Wiebe, *Nat. Phys.* **17**, 943 (2021).
 [11] F. Pientka, L. I. Glazman, and F. von Oppen, *Phys. Rev. B* **88**, 155420 (2013).
 [12] G. C. Ménard, S. Guissart, C. Brun, R. T. Leriche, M. Trif, F. Debontridder, D. Demaille, D. Roditchev, P. Simon, and T. Cren, *Nat. Commun.* **8**, 2040 (2017).
 [13] A. Palacio-Morales, E. Mascot, S. Cocklin, H. Kim, S. Rachel, D. K. Morr, and R. Wiesendanger, *Sci. Adv.* **5**, eaav6600 (2019).
 [14] A. Ptok, D. J. Alspaugh, S. Głodzik, A. Kobińska, A. M. Oleś, P. Simon, and P. Piekarczyk, *Phys. Rev. B* **102**, 245405 (2020).
 [15] J. Linder and J. W. A. Robinson, *Nat. Phys.* **11**, 307 (2015).
 [16] M. Eschrig, *Rep. Prog. Phys.* **78**, 104501 (2015).
 [17] J. W. A. Robinson, J. D. S. Witt, and M. G. Blamire, *Science* **329**, 59 (2010).
 [18] K.-R. Jeon, C. Ciccarelli, A. J. Ferguson, H. Kurebayashi, L. F. Cohen, X. Montiel, M. Eschrig, J. W. A. Robinson, and M. G. Blamire, *Nat. Mater.* **17**, 499 (2018).
 [19] N. Banerjee, J. W. A. Robinson, and M. G. Blamire, *Nat. Commun.* **5**, 4771 (2014).
 [20] A. K. Feofanov, V. A. Oboznov, V. V. Bol'ginov, J. Lisenfeld, S. Poletto, V. V. Ryazanov, A. N. Rossolenko, M. Khabipov, D. Balashov, A. B. Zorin, P. N. Dmitriev, V. P. Koshelets, and A. V. Ustinov, *Nat. Phys.* **6**, 593 (2010).
 [21] I. V. Vernik, V. V. Bol'ginov, S. V. Bakurskiy, A. A. Golubov, M. Y. Kupriyanov, V. V. Ryazanov, and O. A. Mukhanov, *IEEE Trans. Appl. Supercond.* **23**, 1701208 (2013).
 [22] S. Parkin and S.-H. Yang, *Nat. Nanotechnol.* **10**, 195 (2015).
 [23] Z. Luo, A. Hrabec, T. Phuong Dao, G. Sala, S. Finizio, J. Feng, S. Mayr, J. Raabe, P. Gambardella, and L. J. Heyderman, *Nature (London)* **579**, 214 (2020).
 [24] A. B. Odobesko, S. Haldar, S. Wilfert, J. Hagen, J. Jung, N. Schmidt, P. Sessi, M. Vogt, S. Heinze, and M. Bode, *Phys. Rev. B* **99**, 115437 (2019).
 [25] A. Odobesko, D. Di Sante, A. Kowalski, S. Wilfert, F. Friedrich, R. Thomale, G. Sangiovanni, and M. Bode, *Phys. Rev. B* **102**, 174504 (2020).
 [26] F. Küster, A. M. Montero, F. S. M. Guimarães, S. Brinker, S. Lounis, S. S. P. Parkin, and P. Sessi, *Nat. Commun.* **12**, 1108 (2021).
 [27] L. Schneider, P. Beck, J. Neuhaus-Steinmetz, L. Rózsa, T. Posske, J. Wiebe, and R. Wiesendanger, *Nat. Nanotechnol.* (2022), doi:10.1038/s41565-022-01078-4.
 [28] S.-H. Ji, T. Zhang, Y.-S. Fu, X. Chen, J.-F. Jia, Q.-K. Xue, and X.-C. Ma, *Appl. Phys. Lett.* **96**, 073113 (2010).
 [29] E. Mascot, J. Bedow, M. Graham, S. Rachel, and D. K. Morr, *npj Quantum Mater.* **6**, 6 (2021).

- [30] J. Bedow, E. Mascot, T. Posske, G. S. Uhrig, R. Wiesendanger, S. Rachel, and D. K. Morr, *Phys. Rev. B* **102**, 180504 (2020).
- [31] R. Wiesendanger, *Rev. Mod. Phys.* **81**, 1495 (2009).
- [32] See Supplemental Material at <http://link.aps.org/supplemental/10.1103/PhysRevB.105.L100406> for more details on: sample preparation; acquisition of spin-resolved STM images; numerical deconvolution of superconductor-vacuum-superconductor spectra; first-principles calculations.
- [33] A. Yazdani, B. A. Jones, C. P. Lutz, M. F. Crommie, and D. M. Eigler, *Science* **275**, 1767 (1997).
- [34] V. Madhavan, W. Chen, T. Jamneala, M. F. Crommie, and N. S. Wingreen, *Science* **280**, 567 (1998).
- [35] K. J. Franke, G. Schulze, and J. I. Pascual, *Science* **332**, 940 (2011).
- [36] L. Schneider, M. Steinbrecher, L. Rózsa, J. Bouaziz, K. Palotás, M. dos Santos Dias, S. Lounis, J. Wiebe, and R. Wiesendanger, *npj Quantum Mater.* **4**, 42 (2019).
- [37] S. Brinker, F. Küster, S. S. P. Parkin, P. Sessi, and S. Lounis, *Sci. Adv.* **8**, eabi7291 (2022).
- [38] J.-D. Pillet, C. H. L. Quay, P. Morfin, C. Bena, A. L. Yeyati, and P. Joyez, *Nat. Phys.* **6**, 965 (2010).
- [39] D.-J. Choi, C. Rubio-Verdú, J. de Bruijckere, M. M. Ugeda, N. Lorente, and J. I. Pascual, *Nat. Commun.* **8**, 15175 (2017).
- [40] R. C. Dynes, V. Narayanamurti, and J. P. Garno, *Phys. Rev. Lett.* **41**, 1509 (1978).
- [41] J. A. Stroschio and R. J. Celotta, *Science* **306**, 242 (2004).
- [42] M. Bode, S. Heinze, A. Kubetzka, O. Pietzsch, M. Hennefarth, M. Getzlaff, R. Wiesendanger, X. Nie, G. Bihlmayer, and S. Blügel, *Phys. Rev. B* **66**, 014425 (2002).
- [43] R. Drautz and M. Fähnle, *Phys. Rev. B* **69**, 104404 (2004).
- [44] J. Zabloudil, R. Hammerling, L. Szunyogh, and P. Weinberger, *Electron Scattering in Solid Matter: A Theoretical and Computational Treatise* (Springer, Berlin, Heidelberg, 2005).
- [45] G. Kresse and J. Furthmüller, *Comput. Mater. Sci.* **6**, 15 (1996).
- [46] G. Kresse and J. Furthmüller, *Phys. Rev. B* **54**, 11169 (1996).
- [47] J. Hafner, *J. Comput. Chem.* **29**, 2044 (2008).
- [48] J. P. Perdew, K. Burke, and M. Ernzerhof, *Phys. Rev. Lett.* **77**, 3865 (1996).
- [49] L. Szunyogh, L. Udvardi, J. Jackson, U. Nowak, and R. Chantrell, *Phys. Rev. B* **83**, 024401 (2011).
- [50] A. Deák, L. Szunyogh, and B. Ujfalussy, *Phys. Rev. B* **84**, 224413 (2011).
- [51] B. Schweflinghaus, B. Zimmermann, M. Heide, G. Bihlmayer, and S. Blügel, *Phys. Rev. B* **94**, 024403 (2016).
- [52] E. Simon, L. Rózsa, K. Palotás, and L. Szunyogh, *Phys. Rev. B* **97**, 134405 (2018).
- [53] M. Bode, M. Heide, K. Von Bergmann, P. Ferriani, S. Heinze, G. Bihlmayer, A. Kubetzka, O. Pietzsch, S. Blügel, and R. Wiesendanger, *Nature (London)* **447**, 190 (2007).
- [54] M. T. Mercaldo, P. Kotetes, and M. Cuoco, *AIP Adv.* **8**, 101303 (2018).
- [55] S. Manna, A. Kamlapure, L. Cornils, T. Hänke, E. M. J. Hedegaard, M. Bremholm, B. B. Iversen, P. Hofmann, J. Wiebe, and R. Wiesendanger, *Nat. Commun.* **8**, 14074 (2017).
- [56] P. G. De Gennes, *Superconductivity of Metals and Alloys*, translated by P. A. Pincus, 1st ed. (CRC Press, Boca Raton, 1999).